JOURNAL OF SYNCHROTRON RADIATION
ISSN 1600-5775

Using synchrotron radiation inline phase-contrast imaging computed tomography to visualize three-dimensional printed hybrid constructs for cartilage tissue engineering

Adeola D. Olubamiji,[a]* Zohreh Izadifar,[a] Ning Zhu,[b] Tuanjie Chang,[c] Xiongbiao Chen[a] and B. Frank Eames[a,c]*

[a]Biomedical Engineering, University of Saskatchewan, 57 Campus Drive, Saskatoon, Saskatchewan, Canada S7N 5A9, [b]Canadian Light Source, 44 Innovation Boulevard, Saskatoon, Saskatchewan, Canada S7N 2V3, and [c]Anatomy and Cell Biology, University of Saskatchewan, 107 Wiggins Road, Saskatoon, Saskatchewan, Canada S7N 5E5. *Correspondence e-mail: ade.ola@usask.ca, b.frank@usask.ca

Received 2 December 2015
Accepted 7 February 2016

Edited by J. F. van der Veen

Keywords: SR-inline-PCI-CT; sample-to-detector distance; hybrid constructs; cartilage tissue engineering.

Synchrotron radiation inline phase-contrast imaging combined with computed tomography (SR-inline-PCI-CT) offers great potential for non-invasive characterization and three-dimensional visualization of fine features in weakly absorbing materials and tissues. For cartilage tissue engineering, the biomaterials and any associated cartilage extracellular matrix (ECM) that is secreted over time are difficult to image using conventional absorption-based imaging techniques. For example, three-dimensional printed polycaprolactone (PCL)/alginate/cell hybrid constructs have low, but different, refractive indices and thicknesses. This paper presents a study on the optimization and utilization of inline-PCI-CT for visualizing the components of three-dimensional printed PCL/alginate/cell hybrid constructs for cartilage tissue engineering. First, histological analysis using Alcian blue staining and immunofluorescent staining assessed the secretion of sulfated glycosaminoglycan (GAGs) and collagen type II (Col2) in the cell-laden hybrid constructs over time. Second, optimization of inline PCI-CT was performed by investigating three sample-to-detector distances (SDD): 0.25, 1 and 3 m. Then, the optimal SDD was utilized to visualize structural changes in the constructs over a 42-day culture period. The results showed that there was progressive secretion of cartilage-specific ECM by ATDC5 cells in the hybrid constructs over time. An SDD of 3 m provided edge-enhancement fringes that enabled simultaneous visualization of all components of hybrid constructs in aqueous solution. Structural changes that might reflect formation of ECM also were evident in SR-inline-PCI-CT images. Summarily, SR-inline-PCI-CT images captured at the optimized SDD enables visualization of the different components in hybrid cartilage constructs over a 42-day culture period.

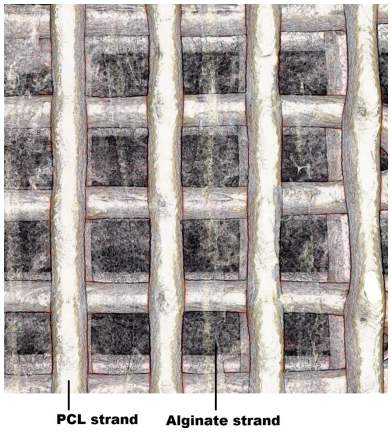

1. Introduction

Three-dimensional printed hybrid constructs fabricated from polycaprolactone (PCL), alginate hydrogel and living cells can mimic the multi-composite and biphasic nature of articular cartilage. Therefore, they have attracted attention for cartilage tissue engineering (CTE) applications (Schuurman *et al.*, 2011; Kundu *et al.*, 2013; Izadifar *et al.*, 2016). However, PCL, alginate hydrogel and embedded cells found in these hybrid constructs have low but different refractive indices and thicknesses. Alginate hydrogel is a hydrophilic, anionic polysaccharide comprising 97.5% water, whereas the PCL component is a hydrophobic, polyester-based solid. Furthermore, newly forming cartilage tissues are often not as thick as native articular cartilage. All of these features make it chal-

lenging to non-invasively characterize architecture of the different components of these constructs, let alone progression of associated tissue growth within the constructs in a fluid-filled environment, without the use of contrast agent (Zehbe *et al.*, 2015; Sun *et al.*, 2011; Appel *et al.*, 2015). Histological examinations complemented by two-dimensional imaging techniques are used typically for standard quantitative and qualitative assessments of tissue-engineered constructs (Boskey & Camacho, 2007; Huebsch & Mooney, 2007; Matsumoto, 2002). Unfortunately, histological examinations are invasive and destructive, involving chemical fixation, paraffin- or resin-embedding and sample staining, all of which might introduce artifacts. Therefore, these methods are not suitable for three-dimensional, non-invasive and longitudinal monitoring of material degradation or cartilage growth of engineered constructs in live animals.

Three-dimensional optical imaging techniques, such as confocal microscopy, optical coherence tomography and Raman spectroscopy, have been explored as alternatives to two-dimensional analysis for tissue engineering applications (Hofmann *et al.*, 2012; Ahearne *et al.*, 2008; Huzaira *et al.*, 2001; Muller & Zumbusch, 2007). However, penetration depth and the need for contrast agents to enhance sensitivity have placed limitations on these methods for CTE applications (Appel *et al.*, 2015). Currently, magnetic resonance imaging (MRI) is the prevalent non-invasive imaging technique to characterize cartilage, scaffolds and associated tissue growth (Potter *et al.*, 2000; Wagner *et al.*, 2005; Prang *et al.*, 2006; Izadifar *et al.*, 2014; Othman *et al.*, 2012). Nevertheless, MRI cannot provide three-dimensional microstructure (Prang *et al.*, 2006), owing to limited spatial and temporal resolution, and cannot resolve well multi-density samples, such as partly hydrophobic and partly hydrophilic samples. For example, even a 17.6 T MRI scanner could not visualize microstructural features of an alginate-based, highly anisotropic capillary hydrogel in the injured spinal cord (Prang *et al.*, 2006). Other non-invasive techniques, such as X-ray micro-computed tomography (micro-CT) enable high-resolution imaging of scaffolds with high refractive indices (Cartmell *et al.*, 2004), but micro-CT provides poor imaging contrast of samples with low refractive indices and high water content, such as alginate hydrogel (van Lenthe *et al.*, 2007).

Synchrotron radiation inline phase-contrast imaging combined with computed tomography (SR-inline-PCI-CT) enables three-dimensional, non-invasive characterization of tissues and constructs with weak X-ray absorption and low refractive indices, making it very useful for CTE applications (Zhu *et al.*, 2015; Murrie *et al.*, 2015; Sun *et al.*, 2011; Izadifar *et al.*, 2014). Compared with conventional X-ray absorption imaging techniques, inline-PCI provides an imaging signal due to refraction (*i.e.* a phase shift in the transmitted X-rays) that is up to 1000 times greater (Davis *et al.*, 1995). Taking advantage of high lateral (spatial) coherence, the advanced refraction-based X-ray imaging technique uses an edge-enhancement property to characterize interfaces between different materials (*e.g.* PCL, alginate hydrogel, cartilage tissue and surroundings; Zhou & Brahme, 2008). Critical for CTE research, inline-PCI can characterize low-density scaffolds and soft tissues (Izadifar *et al.*, 2014; Zhu *et al.*, 2011; Takashima *et al.*, 2015). However, its capability for delineation of fine details was declared inferior to other phase-contrast based methods, such as diffraction-enhanced imaging (Zhu *et al.*, 2011; Sun *et al.*, 2011; Izadifar *et al.*, 2014). Contrast agents, which may affect the functionality of cells in CTE, were used in some cases to enhance imaging contrast of inline-PCI for characterization of samples with low refractive indices (Zehbe *et al.*, 2015). Mainly, inline-PCI-CT has been used to visualize samples with a high refractive index, such as bone (Appel *et al.*, 2015; Sun *et al.*, 2011). Inspired by these previous studies, we hypothesize that inline-PCI can be optimized for characterization of samples with a low refractive index, a critical issue for monitoring the successful application of soft-tissue engineering.

In principle, the X-ray source and the sample-to-detector propagation distance (SDD) play important roles in achieving high spatial coherence of the incident X-rays (Spanne *et al.*, 1999; Murrie *et al.*, 2014; Wilkins *et al.*, 1996). With focus on the effect of SDD, the SDD should fall in the Fresnel zone, a region between near-field and Fraunhofer zones, in order to achieve excellent spatial coherence and diffraction fringes (Zhou & Brahme, 2008). Fresnel diffraction fringes become visible as you progress from the near field to the Fresnel zone, causing edge enhancement at interfaces of different sample components and increasing image contrast. Moreover, penumbral blurring and degradation of image quality occur on progression from the Fresnel to the Fraunhofer zone (Wilkins *et al.*, 1996; Murrie *et al.*, 2014; Zhou & Brahme, 2008). Refractive indices and thickness of the sample, pixel size of the detector, and the imaging energy used for acquiring inline-PCI images also determine the optimum SDD, and may contribute to the shift in SDD at which blurriness starts to occur (Jia *et al.*, 2012).

A few studies have explored the SDD as a key parameter for optimization of inline-PCI for imaging of samples with varying densities and refractive indices. The SDD used for image acquisition determines whether the image contrast obtainable will be absorption or phase contrast (Zhu *et al.*, 2011). For example, for a PLLA/chitosan scaffold imaged in air at 20 keV, an SDD of 2 cm was identified as the absorption-based imaging region and an SDD of 72 cm was identified as the phase-based imaging region (Zhu *et al.*, 2011). Sets of nylon threads imaged at 12 keV, 11 µm pixel size and SDDs ranging from 0 to 1.63 m demonstrated that edge contrast at 0.4 m could delineate fine structural details, which became vague at a 1.155 m or higher SDD (Jia *et al.*, 2012). Similarly, imaging of mouse lung 'speckles', a low-density tissue, at 30 keV, 6.5 µm pixel size and four different SDDs in the range 0.25–5.98 m demonstrated that SDDs in the range 1–4 m were effective (Murrie *et al.*, 2014). The confirmation of effects of SDD on the spatial coherence of X-rays, on edge enhancement at interfaces of materials within samples, and consequently on image quality by these studies were explicit and convincing. However, most of these samples were imaged in air, which resulted in excellent phase contrast and, thereby,

making it easier to delineate material interfaces. Imaging low-density materials surrounded by fluid or tissues of similar density or X-ray attenuation is challenging. Specifically for hybrid cartilage constructs, immersion in fluid makes the generation of huge phase contrast within the biomaterials difficult, because the attenuation coefficients of PCL, alginate hydrogel (with 97.5% water content) and growing cartilage-specific extracellular matrix cartilage (ECM) are all low and close to that of water. Coupled with that, optimization of the SDD for inline-PCI-CT characterization of material degradation or tissue growth during engineering of cartilage tissues has not been carried out.

In the present study, we printed multi-density hybrid constructs, comprising PCL and chondrocyte-impregnated alginate hydrogel, and cultured them up to 42 days *in vitro*. Cell viability as well as secretion of sulfated glycosaminoglycans (GAGs) and collagen type 2 (Col2), which are produced by chondrocytes during the formation of hyaline cartilage (Eames *et al.*, 2003), were analyzed over time of culture. Then, we optimized inline-PCI-CT for visualization of multi-density hybrid constructs in fluid (to better mimic non-invasive assessment in a physiological condition) by varying the SDD from 0.25 to 3 m. The most suitable SDD was utilized for characterization of the overall architecture and structural changes, which might be due to secretion of cartilage-specific ECM, in the hybrid constructs over 42 days of culture. Our findings demonstrate the utility of SR-inline-PCI-CT for non-invasive monitoring of soft tissues, especially for CTE applications.

2. Materials and methods

2.1. Design and biofabrication of PCL/alginate/ATDC5 cells constructs

Using the *Magics Envisiontec* (v13, Materialize, Belgium) software, we designed two computer-aided design (CAD) models to be made from PCL and alginate hydrogel–cell mixture, respectively, and combined them together to create one for the hybrid construct with an oversize of 10 mm × 10 mm × 0.96 mm. The combined model was then imported into *Bioplotter RP* (v2.9, Envisiontec GmbH, Germany) for slicing the bulk structure into four layers, each featured by cylindrical strands with 1 mm inter-strand spacing and 0–90° perpendicular pattern. The sliced model was eventually imported into *VisualMachine* (BP, v2.2, Envisiontec GmbH, Germany) for fabricating the hybrid constructs on a three-dimensional bioplotter (Envisiontec GmbH, Germany). PCL (average M_w ~45000), alginic acid sodium salt [medium viscosity alginate (MVA)], calcium chloride dehydrate ($CaCl_2$), 4-(2-hydroxyethyl)-1-piperazineethanesulfonic acid (HEPES) buffer, mouse chondrogenic cell line ATDC-5 and Stemline® Keratinocyte Medium II calcium free (SKM) were all purchased from Sigma-Aldrich (St Louis, MO, USA) and the hybrid constructs were fabricated in a sterile environment as previously described by Izadifar *et al.* (2016). Briefly, PCL was fed into the syringe of a high-temperature dispensing head, heated up to 358 K and dispensed through a cylindrical metal needle with an inner diameter of 300 µm by using a pneumatic pressure of 0.8 MPa and a deposition speed of 1 mm s^{-1}. An alginate hydrogel (3.3% *w*/*v*) was prepared by dissolving alginic acid sodium salt in the SKM. Then, ATDC-5 cells were suspended in the alginate solution at a density of 8×10^6 cells per ml to make a final concentration of 2.5% *w*/*v* of the alginate–cells solution. The cells–alginate solution was fed into a low-temperature dispensing head and maintained at 283 K. In each layer, PCL strands were first printed using the assigned parameters and then cell-impregnated alginate was dispensed in the spaces between the PCL strands through a conical needle with inner diameter of 200 µm using a pneumatic pressure of 0.03 MPa and a deposition speed of 25 mm s^{-1}. After fabrication of each layer, alginate strands were partially cross-linked using 170 m*M* $CaCl_2$ in 4.2 m*M* HEPES (in 0.35 *M* sucrose) fume released in the direction of the fabrication procedure through an ultrasonic nebulizer (MY-520). After the desired number of layers was reached, the constructs were dipped in 100 m*M* $CaCl_2$ [in 4.2 m*M* HEPES, 0.35 *M* sucrose solution (pH 7.4)] for 20 min to complete cross-linking of the cells–alginate hydrogel network within the PCL framework. After cross-linking, constructs were washed for 5 min in DMEM twice, placed in culture medium in 12-well culture plates, transferred to the incubator and maintained at 310 K and under 5% CO_2. The culture medium was changed every two days: it consisted of DMEM/F-12 HAMs (1:1) supplemented with 5% fetal bovine serum (FBS), penicillin (100 unit per ml), streptomycin (100 µg ml^{-1}), 10 mg ml^{-1} glutamine, 10 mg ml^{-1} insulin–transferrin–selenium plus (ITS+) liquid media supplement and 0.05 mg ml^{-1} ascorbate-2-phosphate (all purchased from Life Technologies). At day zero, 14, 28 and 42 of culture, cultured constructs were collected as described for each assay below.

2.2. Cell viability in hybrid constructs by live/dead assay

The viability of the ATDC-5 cells in the hybrid constructs was examined using a two-colour fluorescence LIVE/DEAD® Kit (Molecular Probes, OR, USA) and fluorescence microscopy at days zero, 14, 28 and 42 of culture as previously described by Izadifar *et al.* (2016). Briefly, the constructs were removed from culture, washed with DMEM for 30 min and submerged in staining solution containing 2 µ*M* calcein-AM and 0.5 µ*M* ethidium homodimer (EthD-1) in DMEM. This procedure was conducted in the dark and constructs were then wrapped in tin foil to prevent any light exposure, then transferred to a 310 K, 5% CO_2 incubator for about 60 min to allow the staining solution to penetrate the layers of the constructs. After 60 min, photomicrographs of stained constructs were taken for live cells (fluoresced green) and dead cells (fluoresced red) using a DP70 camera attached to a Nikon fluorescent inverted microscope (Nikon, ECLIPSE E600, SPOT Insight™ Camera, USA). Then, green and red fluoresced images were merged in *ImageJ* software (Schneider *et al.*, 2012) to localize the distribution of live and dead cells in the constructs. To quantify cell viability, the cells were released

from the constructs by dipping constructs in 1 ml of 50 m*M* EDTA solution to depolymerize alginate hydrogel strands. While protected from light, gentle pipetting was used to pick up 10 µL of the cells suspension onto glass slides and then covered with coverslip. Then, five to six photomicrographs of live and dead cells at different locations on the glass slide were taken using a fluorescent inverted microscope (Nikon, ECLIPSE E600, SPOT Insight™ Camera, USA). The procedure was repeated three times per construct, and live and dead cells from these images were counted for each construct using *ImageJ* software (Schneider *et al.*, 2012).

2.3. Estimation of secretion of sulfated GAGs in constructs by Alcian blue staining

ATDC-5 cells spatially distributed in the hybrid constructs were examined for secretion of sulfated GAGs at days zero, 14, 28 and 42 of culture using Alcian blue staining assay as previously described by Izadifar *et al.* (2016). Hybrid constructs (n = 4 for each time point) were removed from culture, washed in DMEM for 30 min and fixed in methanol: acetone (1:1) on ice for another 30 min. The fixed constructs were stained with 0.5 mg ml^{-1} Alcian blue in 3% acetic acid (pH = 1) and kept overnight at room temperature on a rocker for the stain to penetrate the constructs. The stained constructs were de-stained in 25% ethanol in 3% acetic acid for one hour and stored in 50% ethanol in 3% acetic acid before photomicrographs were obtained using light microscopy. Using *ImageJ* software (Schneider *et al.*, 2012), the regions covered by Alcian blue stains were segmented out of the collected images for further quantitative analysis. Four regions of interest were taken for each construct, and the appropriate threshold was applied to segment the Alcian blue-stained areas of the alginate hydrogel, which were then measured. For each time point, such segmentation was carried out to estimate the area covered by Alcian blue stains compared to the total area of the alginate hydrogel in the regions of interest. These measurements were obtained at the four time points used and compared.

2.4. Estimation of production of Col2 in the hybrid constructs by immunostaining

Secretion of Col2 in the hybrid constructs was examined at days zero, 14, 28 and 42 (n = 4 for each time point) using immunofluorescent staining assay. The hybrid constructs were removed from culture at each time point, fixed in cacodylate buffer [that consists of 200 m*M* sodium cacodylate, 2% paraformaldehyde, 2% glutaraldehyde, and 0.7% ruthenium (III) hexamine trichloride] and incubated for 2 h in 1:100 purified anti-Col2 antibody (purchased from Developmental Studies Hybridoma Bank, Iowa City, USA) in blocking buffer [4% normal goat serum and 2% normal sheep serum in phosphate buffer saline Tween-20 (PBST)]. These constructs were washed 6–8 times in the blocking buffer over a 2 h period after first incubation and then in 1:1000 goat anti-mouse IgG-488 conjugate (purchased from EMD Millipore, Temecula, California, USA) in blocking buffer. After incubation in the secondary antibody, these constructs were washed in PBST over another period of two hours to reduce the background stains and photomicrographs were taken at different positions; horizontally and vertical sections through the constructs, using a DP70 camera attached to fluorescent inverted microscope (Nikon, ECLIPSE E600, SPOT Insight™ Camera, USA). In addition, 0.1 µl ml^{-1} of 4′,6-diamidino-2-phenylindole (DAPI) was added to the immunofluorescent staining assay for DNA labelling of cells to confirm that the cells secreted the Col2 matrix. Similar to the Alcian blue staining, four regions of interest were taken for each construct, and the appropriate threshold was applied to segment the images collected from Col2-stained hybrid constructs at the different time points in *ImageJ* software (Schneider *et al.*, 2012) and used for quantitative measurements.

2.5. SR-inline-PCI-CT of hybrid constructs

Hybrid constructs were fixed at days zero, 14, 28 and 42 of culture in methanol:acetone (1:1) on ice for 20 min and kept in 3% acetic acid for the inline-PCI-CT imaging, performed at the Biomedical Imaging and Therapy-Insertion Device (BMIT-ID) 05ID-2 of the Canadian Light Source using a double-crystal bent Laue monochromator tuned to 30 keV imaging energy (Wysokinski *et al.*, 2015). The hybrid constructs were placed in a sample holder and positioned on the rotating scanning stage for CT imaging. Because calculation of optimum SDD for characterization of multi-density and different low-refractive-indices hybrid constructs have not been previously reported, this study took cues from Lewis *et al.* (2005), Kitchen *et al.* (2008) and Murrie *et al.* (2014, 2015) who reported that an SDD between 1 and 3 m was good for imaging whole mouse lungs and that a SDD greater than 3 m may have negative impact of in-air photon scattering. As a result, tomographic data sets were collected at SDDs of 0.25, 1 and 3 m using a beam monitor AA-60 (Hamamatsu) coupled to a camera C9300 (Hamamatsu) with effective pixel sizes of 8.9, 8.77 and 8.47 µm, respectively. Three thousand projections were collected over a 180° rotation and a set of ten flat-field and ten dark-field images were acquired at the beginning and at the end of each scan to correct the acquired projections. Images of the multi-density hybrid constructs obtained at 0.25, 1 and 3 m SDD were reconstructed and analysed for identification of the optimum SDD. The identified optimum SDD was then used for CT imaging of the hybrid constructs collected from culture at day zero, 14 and 28 (n = 4 for each time point). Phase-retrieved and non-phase-retrieved CT reconstructions of the tomographic data were then performed. *NRecon* (v1.6.10.1; Skyscan, 2011) was used for the non-phase-retrieved CT reconstruction, whereas phase-retrieved CT reconstruction was performed in *PITRE* (v3.1) (Phase-sensitive X-ray Image processing and Tomography Reconstruction). For the non-phase-retrieved reconstruction, flat- and dark-field corrections and image normalization were carried out on the data sets with an *ImageJ* macro plugin before the reconstruction. Then, a modified Feldkamp algorithm was used to obtain image slices. For the phase-retrieved recon-

struction, flat- and dark-field corrections, sinogram generation, phase retrieval and slice reconstruction were all included and carried out in *PITRE* (v3.1) with a phase-attenuation duality Born algorithm (PAD-BA) and $\varepsilon = \delta/\beta = 900$ (Chen *et al.*, 2012). Then, three-dimensional volume rendering was performed after the reconstruction in visualization and analysis software *Avizo* (v9; FEI Visualization Sciences Group, Düsseldorf, Germany), without decomposing the images into geometric primitives, to support the two-dimensional greyscale information of the reconstructed slices.

2.6. Statistical analysis

All statistical tests were performed with *SPSS* (released 2013 IBM SPSS Statistics for Windows, v21.0. Armonk, NY: IBM Corp.). For the Alcian blue staining and the Col2 staining, measurements from the analysis were performed in *ImageJ* software (Schneider *et al.*, 2012) to quantify secretion of GAGs and Col2, respectively. Five different images of each construct ($n = 4$ for each time point) were captured and used for each analysis. Repeated measures analysis of variance (ANOVA) was used to determine the change in area stained over time. *Post hoc* tests using the Bonferroni correction were conducted to estimate the statistical significance between these areas over time. The value of $P < 0.05$ was considered statistically significant.

3. Results

3.1. Cell viability of hybrid constructs remained high at all time points

Viability of the ATDC-5 cells impregnated in the hybrid constructs ($n = 4$ for each time point) was estimated over time of culture using a two-colour fluorescence LIVE/DEAD® Kit (Molecular Probes, OR, USA). Cells were distributed uniformly throughout the hybrid constructs and their viability was 84.4 ± 2.2% at day zero. At day 14, cell viability reduced to 77.2 ± 2.1% and increased to 84.3 ± 2.8% at day 28 and 85.0 ± 5.4% at day 42 (Fig. 1). Cells in the alginate hydrogel strands of the hybrid constructs formed clusters or aggregates, which increased in size, from day 14 onwards (Figs. 1B–1D). Moreover, cross-section images obtained by cutting transversely the centre of the constructs at day 14 and 28 showed that cells in the middle of constructs had comparable spatial distribution and viability to the cells in the periphery (Figs. 1E–1F).

3.2. Secretion of sulfated GAGs in hybrid constructs increased over time

Secretion of sulfated GAGs in the three-dimensional printed cell-impregnated hybrid constructs was examined by Alcian blue staining at the four time points (Fig. 2). The blue-stained area was well dispersed and darkened over time, reflecting a progressive increase in the production of sulfated GAGs in the ECM (Figs. 2A–2H). Cross-section views of the constructs also indicated that secretion of sulfated GAGs was distributed in the inner layers of the constructs (Figs. 2I–2L). Using one-way repeated measures ANOVA with sphericity assumed, the mean area covered by the Alcian blue stains in the hybrid constructs differed with statistical significance between time points [F (3, 9) = 113.194, $P < 0.001$]. *Post hoc* tests using the Bonferroni correction (graphically presented in Fig. 2) showed a statistically significant difference between day zero and day 14 (p-value = 0.011), day zero and day 28 (p-value = 0.005), day zero and day 42 (p-value = 0.001), and day 14 and day 42 (p-value = 0.030).

3.3. Estimation of secretion of Col2 in the hybrid constructs

Secretion of Col2 in the hybrid constructs was examined at days zero, 14, 28 and 42 ($n = 4$ for each time point) using immunofluorescence. Similar to the Alcian blue staining results, secretion of Col2 increased progressively from day zero to day 42 (Figs. 3A–3D). DAPI staining reflected the locations of cells in the Col2-positive areas (Figs. 3E–3H). Cross-section views of the transected constructs indicated that secretion of Col2 also occurred in the inner layers of the constructs (Figs. 3I–3L). In addition, high-magnification views

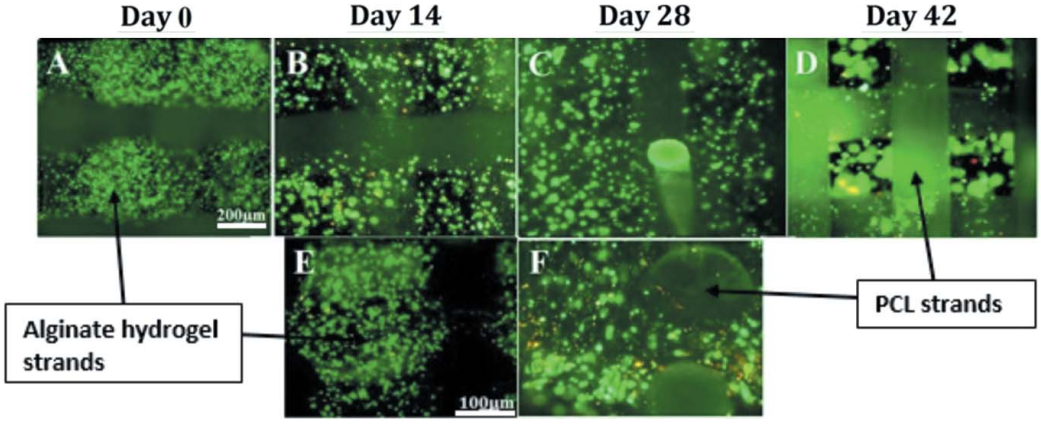

Figure 1
Fluorescent microscopy images of merged live (green) and dead (red) ATDC-5 cells spatially distributed in hybrid constructs at day 0–42: panels A–D are images looking down on the intact constructs over the entire culture period, whereas panels E and F are cross-section images through the centre of the hybrid constructs at day 14 and 28.

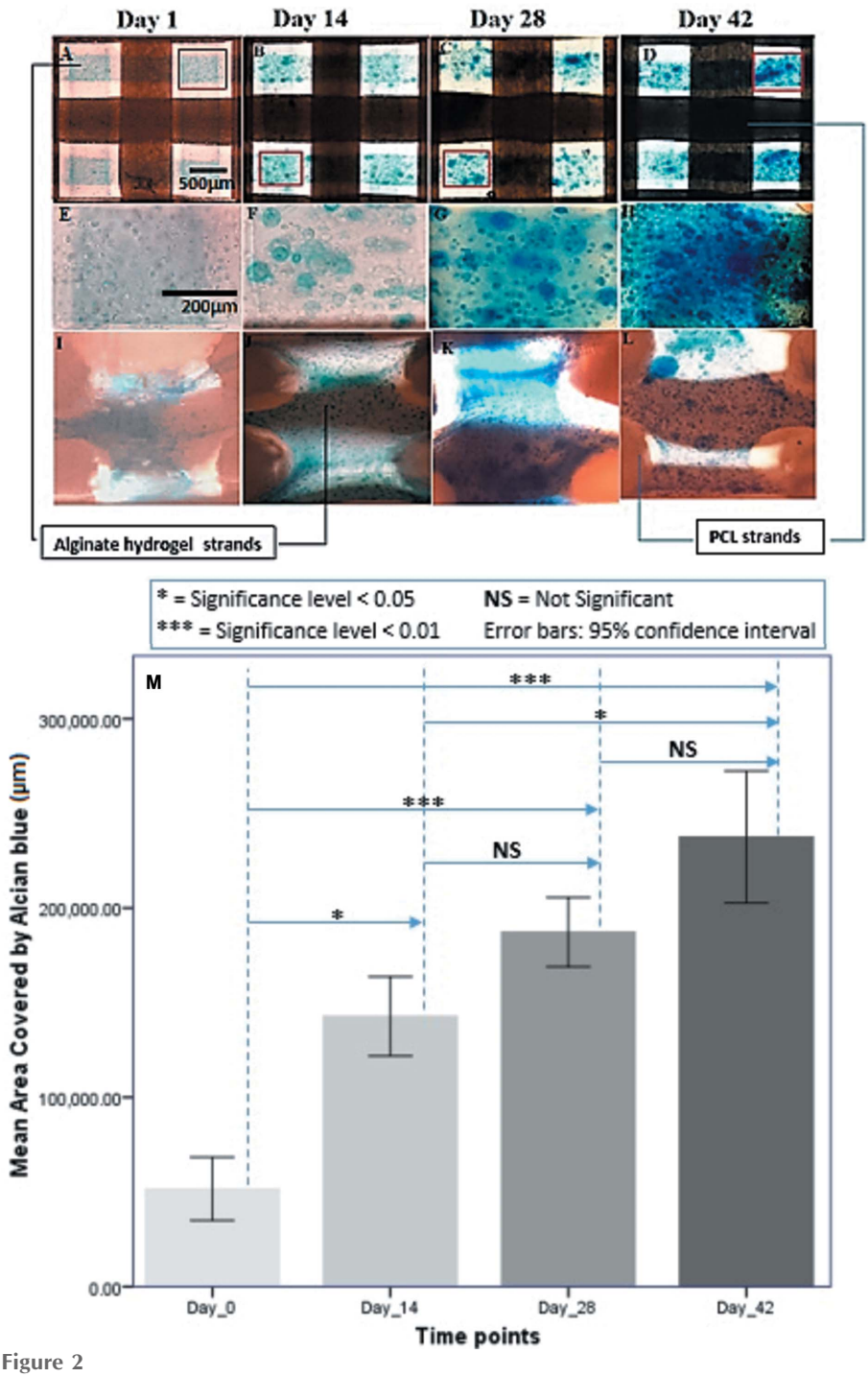

Figure 2
Comparison of Alcian blue staining in three-dimensional printed cell-impregnated constructs, showing secretion of sulfated GAGs at different time points. Panels A–D demonstrate progressive secretion of sulfated GAGs, and E–H are high-magnification views of the regions of interest highlighted in the red boxes of panels A–D. Panels I–L are cross-section images through the centre of the hybrid constructs. Panel M represents the quantitative analysis of Alcian blue stained area in the hybrid constructs at days zero, 14, 28 and 42 showing statistically significant difference in secretion of GAGs at the different time points.

of constructs cultured for 42 days showed that clusters of cells secreting matrix were present in alginate hydrogel strands and also around the PCL strands (Figs. 3M–3P), suggesting that some cells in the alginate migrated to the PCL strands and secreted Col2 matrix. One-way repeated measures ANOVA with sphericity assumed demonstrated that the mean area covered by Col2 staining was significantly different between time points [F (3, 9) = 207.021, P < 0.001]. In fact, *post hoc* tests using Bonferroni correction (graphically presented in Fig. 3) revealed that secretion of Col2 over time showed a statistically significant difference between day zero and day 14 (p-value = 0.048), day zero and day 28 (p-value = 0.002), day zero and day 42 (p-value = 0.002), day 14 and day 42 (p-value = 0.005) and between day 28 and day 42 (p-value = 0.003).

3.4. Effect of SDD on visualizing the different components of the hybrid constructs

Non-phase-retrieved and phase-retrieved CT reconstruction applications were investigated to determine the reconstruction method that provides better details of the individual components of the multi-density constructs in fluid. CT reconstructions were used to obtain image slices from the imaging data of day 14 hybrid constructs obtained at 3 m. The edge contrast obtained from phase-retrieved images after reconstruction revealed the PCL strands, but could not discriminate the lower-refractive-index alginate hydrogel strands in between the PCL from the surrounding fluid (Figs. 4*a* and 4*c*). On the other hand, the edge contrast obtained from the non-phase-retrieved CT reconstruction clearly delineated the interfaces of all components of the hybrid construct: PCL-fluid, PCL-alginate and alginate-fluid (Figs. 4*b* and 4*d*). Therefore, the edge-enhancement attribute of the non-phase-retrieved CT reconstruction better characterized features of the multi-density, multi-refractive-index hybrid constructs compared with the phase-retrieved CT reconstruction.

As the non-phase-retrieved reconstruction technique of *NRecon* (v1.6.10) provided the details required for characterizing each component of our hybrid constructs, it was used to establish the optimum imaging SDD among those tested: 0.25, 1 and 3 m.

After identifying that the non-phase-retrieved reconstruction technique provided details required for characterization

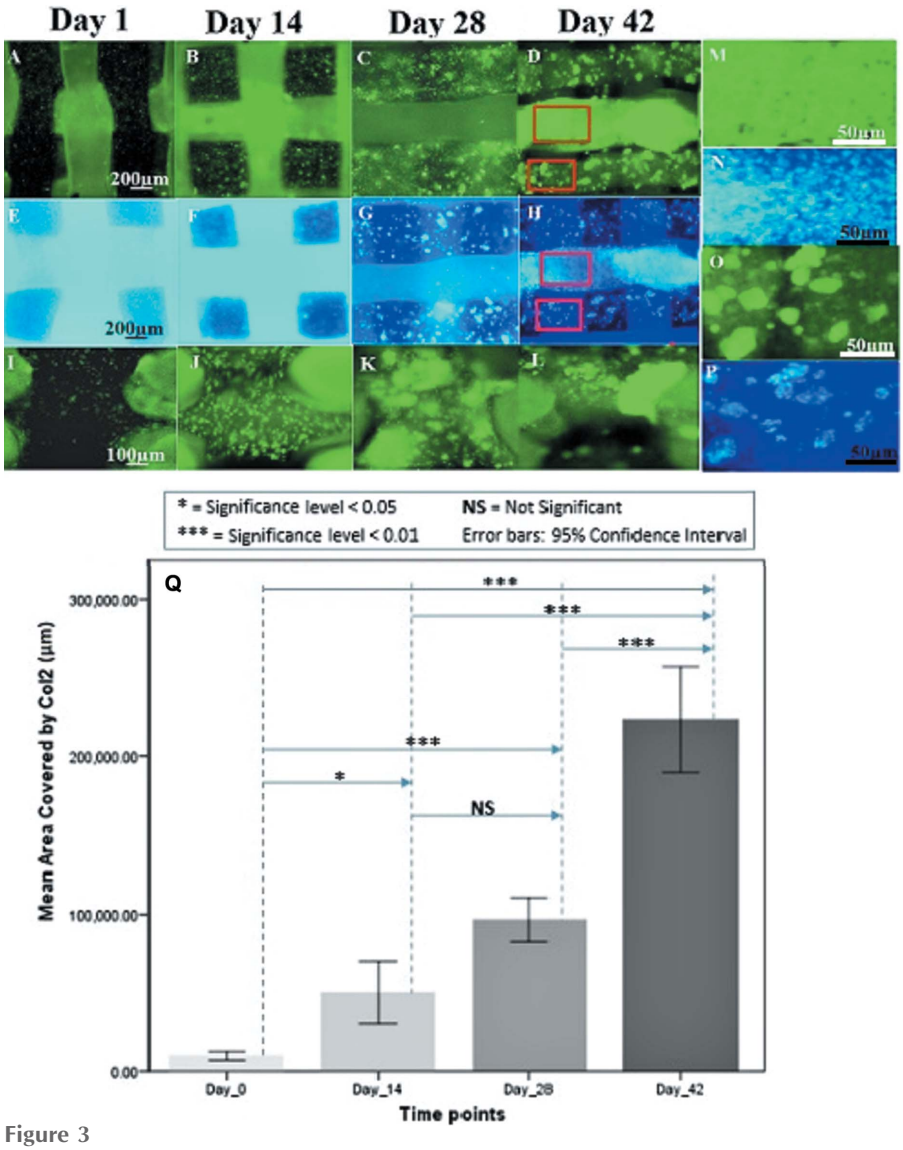

Figure 3
Comparison of Col2 immunostaining and DNA labelling in three-dimensional printed cell-impregnated constructs at different time points. Panels A–D and E–H show progressive secretion of Col2 and corresponding DAPI staining, respectively. Panels I–L are cross-section images through the centre of the hybrid constructs. Panels M and N are high-magnification views of the upper region of interest outlined in red boxes of panels D and H, whereas panels O and P are high-magnification views of the lower region of interest outlined in red boxes of panels D and H. Panel Q represents quantitation of Col2 immunostained area in the hybrid constructs, showing statistically significant differences in Col2 secretion at different time points.

of our multi-component constructs, hybrid construct images obtained from SDDs of 0.25, 1 and 3 m were reconstructed using a non-phase-retrieved reconstruction technique and compared (Fig. 5). Images from the exact same location in a hybrid construct cultured for 42 days were compared [yellow box in Fig. 5(*a*)]. The edge contrast provided at an SDD of 0.25 m identified edges of the PCL strands, but the alginate hydrogel strands were not readily apparent (Figs. 5*b* and 5*e*). At an SDD of 1 m, edges of the PCL strands had higher contrast compared with that obtained at 0.25 m SDD (Figs. 5*c* and 5*f*). In addition, the lower-density alginate strands were faintly visible, due to minimal edge contrast. At an SDD of 3 m, there was an increase in visibility of individual strands and the interfaces between the PCL and alginate hydrogel strands and surrounding fluid (Figs. 5*d* and 5*g*). In particular, the lower-refractive-index and high-water-content alginate hydrogel strands benefited more as the phase contrast more clearly highlighted the edges of these strands.

The distributions of grey values along a line drawn across two PCL strands in the exact same location of the imaged construct were used to quantitate the imaging capabilities of various SDDs [yellow lines in Figs. 5(*b*)–5(*g*)]. Prominent peaks are expected on account of edge contrast or enhancement associated with the difference in refractive indices at material–material or material–fluid interfaces. No high peak was observed from data obtained at 0.25 m SDD (Fig. 5*h*), but two prominent peaks corresponding to the edges of PCL strands were apparent in data obtained at 1 m SDD (Fig. 5*i*). Smaller peaks were also seen between these two prominent peaks that may correspond to the edges of the alginate hydrogel strand. Similar analyses of data obtained at 3 m demonstrated two prominent peaks that corresponded with the edges of PCL strands and other smaller peaks that correspond to the edges of the highly porous alginate hydrogel strand (Fig. 5*j*). The smaller peaks in this case are larger compared with those obtained at 1 m SDD [compare Figs. 5(*i*) and 5(*j*)]. These data demonstrate that the spatial coherence at 3 m SDD provides the most adequate interference fringes among these three SDDs for characterization of each component of the hybrid constructs in aqueous medium.

3.5. SR-inline-PCI-CT reveals structural changes over time in hybrid constructs

Based on the previous data, an SDD of 3 m was used for SR-inline-PCI-CT characterization of structural changes in hybrid constructs at days zero, 14, 28 and 42 ($n = 4$) in culture. Images representing equivalent regions of a limited series of reconstructed slices showed visible structural changes in the constructs during this culture period, especially in the alginate strands (Fig. 6). At days zero and 14, edges of both the PCL and alginate strands appeared uniform from reconstructed images (Figs. 6A and 6B). By day 28, changes in the uniformity of the alginate strands in the constructs were apparent

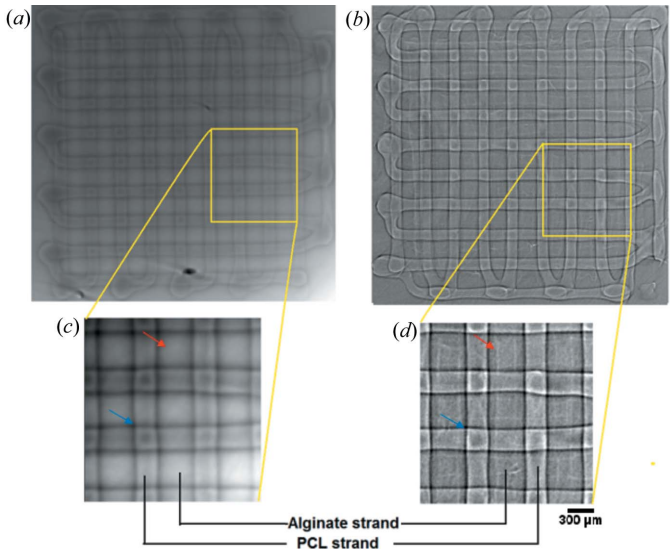

Figure 4
Comparison of output slices of the same image dataset reconstructed using (*a*) phase-retrieved CT reconstruction; (*b*) non-phase-retrieved CT reconstruction; (*c*) magnified region of interest cropped from (*a*); and (*d*) magnified region of interest cropped from (*b*). The PCL strands of the hybrid constructs were visible in both cases. However, alginate hydrogel strands in between the PCL strands were more visible in the non-phase-retrieved image slice than the phase-retrieved image slice. Edge effects show the boundaries of PCL and alginate hydrogel strands in the same location of the hybrid construct (arrow heads).

(Fig. 6C, arrow head). By day 42, the alginate strands were more visible compared with other time points and non-uniform structural changes in the alginate strands were more prominent (Fig. 6D, arrow head).

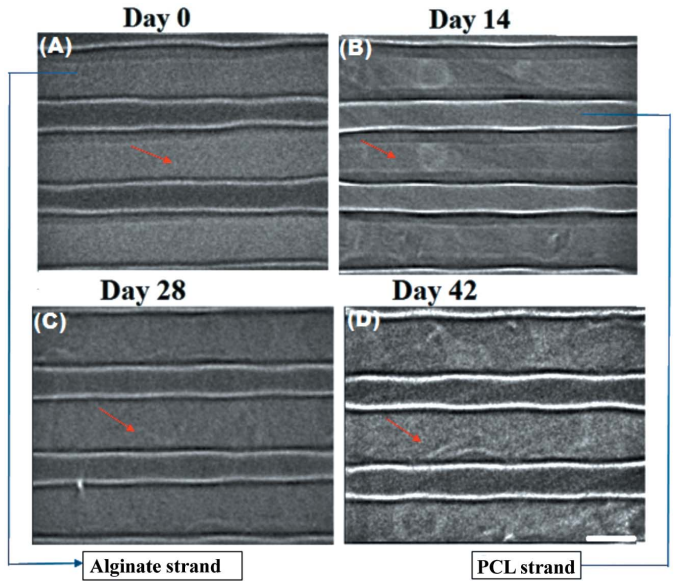

Figure 6
Comparison of SR-inline-PCI-CT images of multi-density hybrid constructs in aqueous medium at the different time points. Images were obtained at 30 keV using 3 m SDD, pixel size of 8.47 µm. Scale bar: 300 µm. Arrow heads show how cell-impregnated alginate strands changed over time.

Three-dimensional volume rendering was performed in *Avizo* (v9) to support the results of the two-dimensional greyscale images and also to provide a three-dimensional image that further showed the different components of the hybrid constructs (day 14 at 3 m SDD). Rendering clearly indicated the interfaces between PCL strands, alginate strands

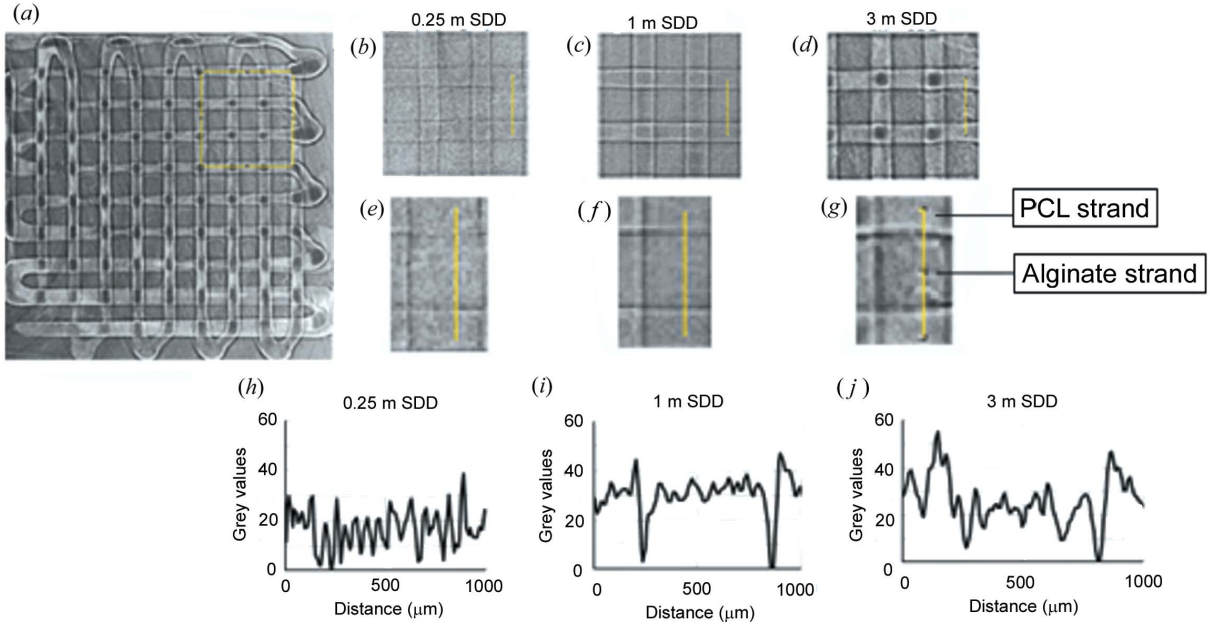

Figure 5
Comparison of inline-PCI-CT images of three-dimensional printed hybrid construct imaged in aqueous medium at three different SDDs. (*a*) Image slice of inline-PCI showing the whole construct imaged at three different SDDs and the region of interest (in yellow box) cropped for analysis of the components of the construct. Inline-PCI-CT image slice obtained at (*b*) 0.25 m SDD, (*c*) 1 m SDD and (*d*) 3 m SDD; (*e*) region of interest cropped out of (*b*) showing the line drawn across two PCL strands; (*f*) region of interest cropped out of (*c*) showing the line drawn across two PCL strands; (*g*) region of interest cropped out of (*d*) showing the line drawn across two PCL strands; (*h*)–(*j*) disribution of grey values in the vicinity of the line shown in (*e*)–(*g*), respectively.

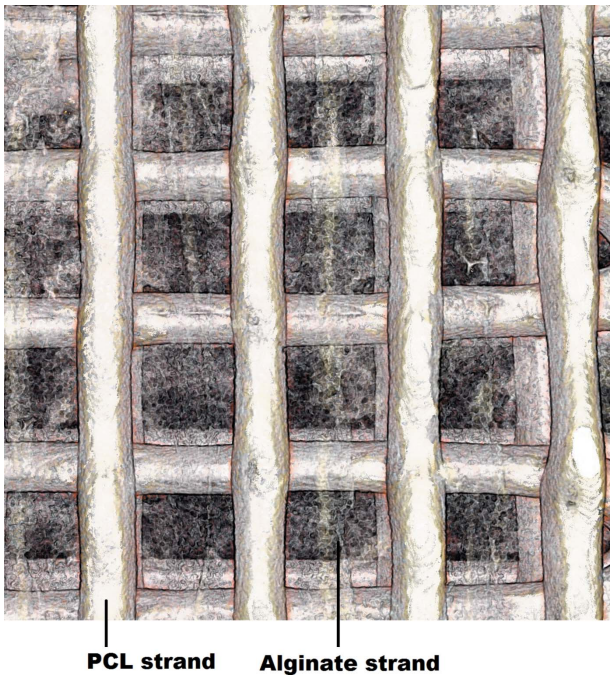

Figure 7
Three-dimensional rendered image of hybrid constructs submerged in fluid showing the interface between PCL strands, alginate hydrogel strands and surrounding fluid.

and surrounding fluid (Fig. 7). Therefore, despite the fact that alginate strands contain 97.5% water and other components of the constructs are submerged in fluid, SR-inline-PCI is capable of providing details of the different low-density and low-refractive-index biomaterial constructs present in the hybrid constructs.

4. Discussion

Non-invasive three-dimensional visualization of the architecture and progression of tissue repair is essential to track the success of various tissue engineering strategies, including those based on three-dimensional printed hybrid construct CTE applications. This is particularly true when the applications are advanced from *in vitro* to *in vivo* and eventually to human studies. The novel technique of SR-inline-PCI-CT enables the characterization of a variety of biomaterials *in vitro* and *in vivo* for tissue engineering applications (Olubamiji *et al.*, 2014; Sun *et al.*, 2011; Zhu *et al.*, 2011, 2015; Zehbe *et al.*, 2015; Izadifar *et al.*, 2014). However, most SR-inline-PCI studies have criticized its capability for delineation of fine details, instead preferring other phase-contrast-based methods, such as diffraction-enhanced imaging (Zhu *et al.*, 2011; Sun *et al.*, 2011; Izadifar *et al.*, 2014). Imaging contrast of inline PCI can be enhanced by a contrast agent (Zehbe *et al.*, 2015), but this may affect (either inhibit or enhance) the functionality of embedded cells (Henning *et al.*, 2009). Other studies mainly focused on characterization of materials with high refractive index, such as bone (Appel *et al.*, 2015; Sun *et al.*, 2011).

In order to optimize SR-inline-PCI-CT for soft tissue engineering applications, this study explored three SDDs, deducing an optimum SDD with excellent edge-enhancement fringes for characterization of each component of multiple low-refractive-index hybrid constructs consisting of PCL, cell-impregnated alginate and surrounding fluid. Increasing the SDD from 0.25 to 3 m resulted in incremental increases in edge contrast and thus increased the ability of SR-inline-PCI-CT to delineate the different components [especially the low-refractive-index cell-impregnated alginate of the multi-density constructs submerged in fluid (Fig. 5)]. However, there was very little phase contrast and thus faint visibility of the alginate strands at SDDs of 0.25 and 1 m. At an SDD of 3 m, the edge-enhancement fringes were optimal among these SDDs, enabling effective characterization of both PCL and alginate components of the constructs submerged in fluid. Though a 4 m SDD was not examined, the edges of PCL strands at a 3 m SDD were already very bright and slightly prone to blurriness, so using an SDD greater than 3 m may not be beneficial for imaging PCL with these particular imaging parameters. Increasing the SDD did provide increasing edge contrast for the lower-refractive-index alginate hydrogel strands, however, so perhaps an SDD greater than 3 m would permit better visualization of alginate. Despite this possibility, previous studies suggest that an SDD larger than 3 m might experience too much photon scattering, producing a negative effect on image contrast (Lewis *et al.*, 2005; Kitchen *et al.*, 2008). In fact, an SDD of 1 m worked better for characterization of airway interfaces of a rat at 30 keV and 12.9 µm when compared with SDDs of 2 or 3 m (Murrie *et al.*, 2014). In addition, the edge contrast of sets of nylon threads imaged at an SDD of 0.4 m using a pixel size of 11 µm provided adequate structural details, which became vague at an SDD of 1.155 m or higher (Jia *et al.*, 2012). That said, all these studies used samples that had a different refractive index. Also, they were not multi-density hybrid samples and were not imaged submerged in fluid. For example, the edge contrast at the interface between alveoli tissues and air will be larger than the interface between alginate strands (containing 97.5% water) and submerged fluid. Also, the optimal SDD depends on the refractive indices found in the sample, the imaging energy and the detector pixel size; therefore, it should be tailored to obtain effective edge-enhancement fringes for each application.

Critically, SR-inline-PCI-CT at a 3 m SDD generated edge enhancement that allowed unparalleled characterization of the overall architecture and structural features of multi-density hybrid constructs in medium. Strands of PCL and alginate were clearly delineated from surrounding fluid in three dimensions, which should greatly increase visualization of *in vivo* integration of tissue constructs (Appel *et al.*, 2015; Zehbe *et al.*, 2015; Sun *et al.*, 2011). The observed micro-structural features in the alginate may reflect changes in density due to either degradation of the alginate (Moya *et al.*, 2012; Takashima *et al.*, 2015) or ECM deposition by the impregnated cells (tissue growth) (Appel *et al.*, 2015; Zehbe *et al.*, 2015; Sun *et al.*, 2011). Regarding the former possibility, X-ray PCI-CT of PGA microfibre scaffolds implanted for

28 days in rats showed that mass density loss caused by degradation resulted in a reduction of the refractive index and density of the implanted scaffold and this consequently caused a reduction in the phase contrast (Takashima *et al.*, 2015). In contrast, the alginate strands in our hybrid constructs did not appear to have lower phase contrast over time and visible mass loss was not evident, even at day 42. Regarding the possibility that the observed microstructural features in the alginate reflected ECM deposition by impregnated cells, increased phase contrast during culture time of hybrid constructs paralleled increased ECM secretion by impregnated ATDC5 cells (Figs. 2 and 3). Indeed, increases in phase contrast were also associated with deposits of mineralized ECM by mesenchymal stem cells in alginate beads during *in vitro* culture (Appel *et al.*, 2015). Future work to resolve this issue should examine exact spatial correlation between observed patterns of ECM secretion and phase contrast.

Furthermore, our data demonstrate that the CT reconstruction method (*i.e.* phase retrieval or non-phase retrieval) might affect subsequent data analyses. Phase retrieval can provide quantitative information (Zhu *et al.*, 2015), but it did not produce better qualitative images in this paper. Importantly, the non-phase-retrieved CT reconstruction provided edge contrasts that enabled clear delineation of interfaces between all components of the hybrid construct: PCL–fluid, PCL–alginate and alginate–fluid. Non-phase-retrieval CT reconstruction is also achievable using *PITRE* (v3.1) and this study also obtained details similar to the non-phase-retrieved CT reconstruction carried out in *NRecon* (v1.6.10.1; data not shown).

Overall, the progressive secretion of sulfated GAGs and Col2 while maintaining high cell viability (Fig. 1) verified that three-dimensional printed hybrid constructs have the capability to develop into articular cartilage (Izadifar *et al.*, 2016). These features were present throughout the full thickness of the constructs, suggesting that the process can be scaled up to the approximate thickness of native articular cartilage, which would make it even easier to characterize using inline-PCI, especially if cultured for longer times (Kundu *et al.*, 2013; Schuurman *et al.*, 2011). Despite the fact that the alginate strands contain 97.5% water and the constructs are immersed in fluid, our study demonstrates that inline-PCI can provide details of the different low-density and low-refractive-index biomaterial constructs and their surroundings. As a result, the promising capability of inline-PCI-CT in visualizing subtle structural changes in these constructs suggests further application of this technique to assessment of larger tissue constructs at much longer culture times *in vitro* and *in vivo*.

5. Conclusions

This study illustrates that SR-inline-PCI-CT offers an unparalleled technique for non-invasive, non-destructive and three-dimensional characterization of overall architecture of the different components of hybrid constructs in aqueous solution, which would be impossible by using absorption-based imaging techniques. For three-dimensional printed samples of PCL and cell-impregnated alginate submerged in fluid, an SDD of 3 m provided the edge-enhancement fringes that enabled effective characterization of each component. Despite the similar refractive indices between alginate hydrogel (contains 97.5% water content) and surrounding fluid, SR-inline-PCI-CT allowed assessment of subtle changes within the cell-impregnated alginate over time. Furthermore, histological analyses demonstrated a progressive increase in secretion of sulfated GAGs and Col2 in the cell-impregnated hybrid constructs over time, confirming the utility of three-dimensional printed hybrid constructs for CTE application. We argue that subtle changes in the inline-PCI-CT images of cell-impregnated alginate strands at later time points reflected ECM secreted in the constructs over time. Therefore, this study reveals the promising potential of SR-inline-PCI-CT for non-invasive, nondestructive, three-dimensional and longitudinal characterization of soft tissues in hybrid constructs.

Acknowledgements

The authors acknowledge the funding for the present research from the Saskatchewan Health Research Fund (SHRF), Canadian Institutes of Health Research (CIHR) and Natural Sciences and Engineering Council of Canada (NSERC). We also acknowledge that images presented in this paper were captured at the Canadian Light Source (CLS), which was supported by the Canadian Foundation for Innovation (CFI), NSERC, the University of Saskatchewan, the Government of Saskatchewan, Western Economic Diversification (WED) Canada and CIHR.

References

Ahearne, M., Bagnaninchi, P. O., Yang, Y. & El Haj, A. (2008). *J. Tissue Eng. Regen. Med.* **2**, 521–524.
Appel, A. A., Larson, J. C., Garson, A. B. III, Guan, H., Zhong, Z., Nguyen, B. B., Fisher, J. P., Anastasio, M. A. & Brey, E. M. (2015). *Biotechnol. Bioeng.* **112**, 612–620.
Boskey, A. & Pleshko Camacho, N. (2007). *Biomaterials*, **28**, 2465–2478.
Cartmell, S., Huynh, K., Lin, A., Nagaraja, S. & Guldberg, R. (2004). *J. Biomed. Mater. Res. A*, **69**, 97–104.
Chen, R.-C., Dreossi, D., Mancini, L., Menk, R., Rigon, L., Xiao, T.-Q. & Longo, R. (2012). *J. Synchrotron Rad.* **19**, 836–845.
Davis, T. J., Gao, D., Gureyev, T. E., Stevenson, A. W. & Wilkins, S. W. (1995). *Nature (London)*, **373**, 595–598.
Eames, B. F., de la Fuente, L. & Helms, J. A. (2003). *Birth Defects Res. C Embryo Today*, **69**, 93–101.
Henning, T. D., Sutton EJ, Kim, A., Golovko, D., Horvai, A., Ackerman, L., Sennino, B., McDonald, D., Lotz, J. & Daldrup-Link, H. E. (2009). *Contrast Media Mol. Imaging*, **4**, 165–173.
Hofmann, M. C., Whited, B. M., Criswell, T., Rylander, M. N., Rylander, C. G., Soker, S., Wang, G. & Xu, Y. (2012). *Tissue Eng. C*, **18**, 677–687.
Huebsch, N. D. & Mooney, D. J. (2007). *Biomaterials*, **28**, 2424–2437.
Huzaira, M., Rius, F., Rajadhyaksha, M., Anderson, R. R. & González, S. (2001). *J. Invest. Dermatol.* **116**, 846–852.
Izadifar, Z., Chang, T., Kulyk, W., Chen, X. B. & Eames, B. F. (2016). *Tissue Eng. C*, **22**, 173–188.

Izadifar, Z., Chapman, L. D. & Chen, X. (2014). *Tissue Eng. C*, **20**, 140–148.
Jia, Q. J., Chen, Y., Li, G. & Jiang, X. (2012). *Chin. Phys. C*, **36**, 267–274.
Kitchen, M. J., Lewis, R. A., Morgan, M. J., Wallace, M. J., Siew, M. L., Siu, K. K. W., Habib, A., Fouras, A., Yagi, N., Uesugi, K. & Hooper, S. B. (2008). *Phys. Med. Biol.* **53**, 6065–6077.
Kundu, J., Shim, J. H., Jang, J., Kim, S. W. & Cho, D. W. (2013). *J. Tissue Eng. Regen. Med.* **9**, 1286–1297.
Lenthe, G. H. van, Hagenmüller, H., Bohner, M., Hollister, S. J., Meinel, L. & Müller, R. (2007). *Biomaterials*, **28**, 2479–2490.
Lewis, R. A., Yagi, N., Kitchen, M. J., Morgan, M. J., Paganin, D., Siu, K. K. W., Pavlov, K., Williams, I., Uesugi, K., Wallace, M. J., Hall, C. J., Whitley, J. & Hooper, S. B. (2005). *Phys. Med. Biol.* **50**, 5031–5040.
Matsumoto, B. (2002). Editor. *Cell Biological Applications of Confocal Microscopy*, Vol. 70. New York: Academic Press.
Moya, M. L., Morley, M., Khanna, O., Opara, E. C. & Brey, E. M. (2012). *J. Mater. Sci.* **23**, 903–912.
Muller, M. & Zumbusch, A. (2007). *ChemPhysChem*, **8**, 2156–2170.
Murrie, R. P., Morgan, K. S., Maksimenko, A., Fouras, A., Paganin, D. M., Hall, C., Siu, K. K. W., Parsons, D. W. & Donnelley, M. (2015). *J. Synchrotron Rad.* **22**, 1049–1055.
Murrie, R. P., Stevenson, A. W., Morgan, K. S., Fouras, A., Paganin, D. M. & Siu, K. K. W. (2014). *J. Synchrotron Rad.* **21**, 430–445.
Olubamiji, A. D., Izadifar, Z. & Chen, D. X. (2014). *Tissue Eng. B*, **20**, 503–522.
Othman, S. F., Curtis, E. T., Plautz, S. A., Pannier, A. K., Butler, S. D. & Xu, H. (2012). *NMR Biomed.* **25**, 452–463.
Potter, K., Butler, J. J., Horton, W. E. & Spencer, R. G. S. (2000). *Arthritis Rheum.* **43**, 1580–1590.
Prang, P., Müller, R., Eljaouhari, A., Heckmann, K., Kunz, W., Weber, T., Faber, C., Vroemen, M., Bogdahn, U. & Weidner, N. (2006). *Biomaterials*, **27**, 3560–3569.
Schneider, C. A., Rasband, W. S. & Eliceiri, K. W. (2012). *Nat. Methods*, **9**, 671–675.
Schuurman, W., Khristov, V., van Pot, M. W., Weeren, P. R., Dhert, W. J. & Malda, J. (2011). *Biofabrication*, **3**, 021001.
Skyscan (2011). *NRecon User Manual*, http://www.skyscan.be/next/NReconUserGuide.pdf.
Spanne, P., Raven, C., Snigireva, I. & Snigirev, A. (1999). *Phys. Med. Biol.* **44**, 741–749.
Sun, W., Li, Z. R., Yang, Y. R., Shi, Z. C., Wang, B., Liu, B. & Shi, S. (2011). *Orthopedics*, **34**, e530–e534.
Takashima, K., Hoshino, M., Uesugi, K., Yagi, N., Matsuda, S., Nakahira, A., Osumi, N., Kohzuki, M. & Onodera, H. (2015). *J. Synchrotron Rad.* **22**, 136–142.
Wagner, A. *et al.* (2005). *Nucl. Instrum. Methods Phys. Res. A*, **548**, 47–53.
Wilkins, S. W., Gureyev, T. E., Gao, D., Pogany, A. & Stevenson, A. W. (1996). *Nature (London)*, **384**, 335–338.
Wysokinski, T., Chapman, D., Adams, G., Renier, M., Suortti, P. & Thomlinson, W. (2015). *Nucl. Instrum. Methods Phys. Res. A*, **775**, 1–4.
Zehbe, R., Schmitt, V. H., Kirkpatrick, C. J. & Brochhausen, C. (2015). *Mater. Sci. Technol.* **31**, 167–173.
Zhou, S. & Brahme, A. (2008). *Phys. Med.* **24**, 129–148.
Zhu, N., Chapman, D., Cooper, D., Schreyer, D. J. & Chen, X. (2011). *Tissue Eng. C*, **17**, 1071–1080.
Zhu, N. A., Rajaram, A., Olubamiji, A. D. J., Schreyer, D. J., Wysokinski, T. W., Belev, G. & Chen, X. B. (2015). *4th TERMIS World Congress*, 8–11 September 2015, Boston, MA, USA.